Constitutive equations for modeling non-Schmid effects in single crystal bcc-Fe at low and ambient temperatures

CrossMark

Anirban Patra [a,*], Ting Zhu [a,b], David L. McDowell [a,b]

[a] School of Materials Science & Engineering, Georgia Institute of Technology, Atlanta, GA 30332, USA
[b] GWW School of Mechanical Engineering, Georgia Institute of Technology, Atlanta, GA 30332, USA

ARTICLE INFO

ABSTRACT

Constitutive equations are developed for single crystal bcc-Fe at low and ambient temperatures based on the assumption that non-Schmid effects are primarily influential on orientation dependence and tension–compression asymmetry of the initial yield stress. Temperature dependence of the non-Schmid parameters is extracted from a fit to available experimental data. Constitutive models are also developed for the decay of the influence of non-Schmid stresses with inelastic deformation. These equations are used in a dislocation density-based crystal plasticity framework to model the mechanical behavior of bcc-Fe. The stress–strain response is modeled and fit to the experimental data at 298 K. Orientation-dependent yield stress and tension–compression asymmetry simulations are compared to available experiments.

© 2014 Elsevier Ltd. All rights reserved.

1. Introduction

Inelastic deformation in bcc metals is characterized by complex slip modes. It has been argued that initial yield is governed by the non-planar core structure of the ½⟨111⟩ screw dislocations leading to non-Schmid yield behavior at low temperatures (Vitek and Paidar, 2008; Vitek, 1992). Atomistic simulations at 0 K and relatively high stresses show that the core structure of the screw dislocation in bcc crystals is not confined to its slip plane but splits into several planes of the ⟨111⟩ zone, significant of which are the {110} family of planes (Duesbery and Vitek, 1998; Vitek, 2004). This effect has been argued to severely limit the mobility of screw dislocations in bcc metals; the dislocation core must again constrict for it to glide. In contrast to Schmid law, the yield stress depends not only on the resolved shear stress on the primary slip system, but also on stress components of the secondary 'non-glide' slip systems (necessary for the dislocation core to constrict) in these crystals (Bassani and Racherla, 2011; Gröger et al., 2008b; Qin and Bassani, 1992a; Vitek et al., 2004a). Further, plastic flow is non-associative, meaning that the yield surface and plastic flow potential are not identical (Bassani and Racherla, 2011; Bassani et al., 2001; Qin and Bassani, 1992b; Vitek et al., 2004b). Tension–compression asymmetry is an additional manifestation of a non-Schmid formulation, particularly in terms of initial yield stress. Non-Schmid effects have been discussed in connection with the majority of the bcc metals at low temperatures, observed for example, in Fe (Chaussidon et al., 2006; Koester et al., 2012; Spitzig and Keh, 1970a), Mo (Gröger et al., 2008a, 2008b; Irwin et al., 1974; Vitek et al., 2004b), Nb and Nb-Mo alloys (Bolton and Taylor, 1972; Christian, 1983; Statham et al., 1970), Ta and Ta-Re alloys (Nawaz and Mordike, 1975).

The present work pursues this line of modeling non-Schmid effects for bcc-Fe at low and ambient temperatures. Constitutive equations are incorporated in a previously developed dislocation density based crystal plasticity framework for bcc

---

* Corresponding author. Tel.: +1 404 894 7769; fax: +1 404 894 8336.
   E-mail address: anirbanpatra@gatech.edu (A. Patra).

metals (Patra and McDowell, 2012) to model the mechanical behavior of Fe single crystals over a range of crystallographic orientations and temperatures, fitting to available experimental data.

2. Background

To account for the influence of non-Schmid stress components on initial yield, Qin and Bassani (1992a) proposed a first order approximation for the critical yield stress, τ_{cr}, as a linear combination of the resolved shear stress and the non-Schmid stresses on slip system α, i.e.,

$$\tau_{cr} = \tau^\alpha + \sum_{i=1}^{N_{ns}} a_i \tau_i^\alpha \tag{1}$$

where τ^α is the resolved shear stress on slip system α, a_i is the non-Schmid coefficient corresponding to the ith non-Schmid stress component, τ_i^α, and N_{ns} is the total number of non-Schmid stress components. Based on atomistic simulations of an isolated ½ $\langle 1\,1\,1 \rangle$ screw dislocation on the {1 1 0} slip plane in Mo and W (Gröger et al., 2008b), for bcc crystals this yield criterion has the form:

$$\tau_{cr} = \boldsymbol{m}^\alpha \cdot \boldsymbol{\sigma} \cdot \boldsymbol{n}^\alpha + a_1 \boldsymbol{m}^\alpha \cdot \boldsymbol{\sigma} \cdot \boldsymbol{n}_{ns}^\alpha + a_2 (\boldsymbol{n}^\alpha \times \boldsymbol{m}^\alpha) \cdot \boldsymbol{\sigma} \cdot \boldsymbol{n}^\alpha + a_3 (\boldsymbol{n}_{ns}^\alpha \times \boldsymbol{m}^\alpha) \cdot \boldsymbol{\sigma} \cdot \boldsymbol{n}_{ns}^\alpha \tag{2}$$

where σ is the current stress state, $\boldsymbol{m}^\alpha$ and $\boldsymbol{n}^\alpha$ are unit vectors corresponding to the slip direction and the slip plane normal on slip system α, $\boldsymbol{n}_{ns}^\alpha$ is the unit vector of the 'non-glide' plane, and, a_1, a_2, and a_3 are coefficients that can be fit to the atomistically/experimentally determined yield stress for the bcc single crystal loaded in different orientations. From left to right, the terms on the RHS of Eq. (2) represent the resolved (Schmid) shear stress along the slip plane, the resolved shear stress along the 'non-glide' plane, the resolved stress normal to the primary slip plane, and the resolved stress normal to the 'non-glide' plane, respectively. For the case of a conventional Schmid-type yield formulation, only the resolved shear stress on the primary slip plane is considered, i.e., $a_1 = a_2 = a_3 = 0$.

In recent years, a number of continuum crystal plasticity frameworks have incorporated non-Schmid effects in bcc crystals at low homologous temperatures (Buchheit et al., 2011; Koester et al., 2012; Lim et al., 2013; Weinberger et al., 2012; Yalcinkaya et al., 2008). These frameworks generally rely on the aforementioned non-Schmid coefficients (or its variants) to capture the asymmetric yield behavior observed in bcc crystals. With the exception of Lim et al. (2013), the non-Schmid coefficients used in these crystal plasticity models are generally assessed using molecular statics simulations performed at 0 K. However, experimental studies of single crystal bcc metals suggest that the contribution of non-Schmid stresses to the yield stress diminishes with increasing temperature. For example, studies on single crystal Fe (Spitzig and Keh, 1970a) show that as the temperature is increased from 143 K, deviation of yield from Schmid's law decreases monotonically and is significantly reduced at 295 K. Based on comparison to experiments, Lim et al. (2013) showed that while the non-Schmid stresses are dominant in the yield behavior of single crystal Ta at 77 K, they are not so significant at 273 K and 300 K. Chen and co-authors (Chen, 2013; Chen et al., 2013) also derived an atomistically based macroscopic yield criterion and an orientation-dependent Peierls potential for kink-pair nucleation on screw dislocations in bcc-Fe. In their bottom-up model, effects of temperature on diminishing the twinning-antitwinning asymmetry and tension–compression asymmetry are captured by the Peierls potential itself. Temperature dependence of the non-Schmid coefficients thus needs to be considered in the expression for yield in constitutive models that employ this kind of non-Schmid formulation.

It should also be noted that the non-Schmid coefficients derived from atomistics are based on simulations of an isolated screw dislocation in the lattice, meaning that the yield stress is simply the lattice frictional resistance that needs to be overcome to initiate glide of an isolated screw dislocation; dislocation–dislocation interactions are not considered. Also, the yield criterion does not provide any information about the evolution of non-Schmid stresses past the point of initial yield. In the presence of the long range field of other dislocations, the contribution of non-Schmid stresses may be expected to diminish beyond the point of initial yield, more so because dislocation glide (plastic flow) is governed primarily by the Schmid stresses. These effects are not generally considered in the continuum crystal plasticity models mentioned above.

The present work develops constitutive equations for yield in bcc-Fe, accounting for the temperature dependence of non-Schmid coefficients, and the evolution of non-Schmid stresses with inelastic deformation. These equations are coupled with existing models for thermally-activated dislocation glide kinetics and used in a dislocation density based crystal plasticity framework (Patra and McDowell, 2012) to model the orientation and temperature dependence of yield and inelastic flow in single crystal Fe. A top-down modeling approach is presented, with model parameters based on available experimental data from laboratory scale coupons. Much experimental and modeling work still remains to resolve the complexity of dislocation mobility and initial yield phenomena in bcc crystals. Alternative explanations may be offered and pursued for orientation dependence and rate dependence of initial yield in bcc crystals that relates to complex dislocation kink-pair phenomena that govern kinetics at low applied stress levels and finite temperature without resorting to the non-Schmid effects in Eq. (2) (i.e., $a_1 = a_2 = a_3 = 0$, cf. Narayanan et al. (2014)). This line of reasoning would require that tension–compression asymmetry arise more from cooperative mesoscale (many body) manifestations of the intrinsic twinning-antitwinning asymmetry of the orientation dependent Peierls stress of bcc crystals. The distinction and validity of these two very different frameworks for mobility of screw dislocations in bcc crystals will take more time to fully resolve. In the present work, we

consider available experimental data to explore the temperature dependence and consistency of the formulation based on non-Schmid effects.

3. Temperature dependence of non-Schmid coefficients

As mentioned earlier, inelastic deformation in bcc crystals occurs due to the glide of ½ ⟨1 1 1⟩ screw dislocations via kink-pair formation on the {1 1 0} family of planes. The 'non-Schmid' plane corresponding to each of the possible slip systems in bcc crystals is given in Gröger et al. (2008b). It should be noted that the present work deals with modeling the deformation of bcc crystals at low homologous temperatures, in particular room temperature and below. There are contradictory claims in the literature regarding the nature of active slip systems in bcc-Fe at these temperatures. Although the majority of the studies (Caillard, 2010a, 2010b; Gilbert et al., 2011; Koester et al., 2012) concluded that elementary slip occurs via kink-pair formation on the {1 1 0} plane at room temperature and below, Brunner and Diehl (1991a,b) deduced that while this is true at temperatures below 250 K, kink-pair formation occurs on the {1 1 2} plane at temperatures above 250 K. Nonetheless, it has been found (Caillard, 2010a; Gilbert et al., 2011; Marichal et al., 2013) that slip on the {1 1 2} plane is a combination of elementary slip steps on {1 1 0} planes. In the present work, we assume that {1 1 0} planes are the primary slip planes in bcc-Fe. Further, in order to account for the twinning-antitwinning asymmetry observed in bcc crystals (cf. Christian (1983)), forward and backward slip has been explicitly accounted for in Gröger et al. (2008b) by considering the positive and negative slip directions as separate slip systems. Thus, in place of the 12 {1 1 0} ⟨1 1 1⟩ slip systems, we now have 24 slip systems considering both the positive and negative slip directions. The non-Schmid planes corresponding to these slip systems are also given in Gröger et al. (2008b).

The Schmid and non-Schmid stresses (on each slip system) scale linearly as a function of the uniaxial stress, proportional to the respective Schmid and 'non-Schmid' factors. At yield, the slip system with the highest Schmid factor is activated; 'non-Schmid' factors corresponding to the loading orientation can be easily obtained for this activated slip system. Orientation-dependent variation of the uniaxial yield stress may thus be used to estimate the parameters, a_1, a_2, a_3, and τ_{cr}, simultaneously either by solving a system of linear equations corresponding to each orientation for Eq. (2), or using a regression analysis. However, this method predicted non-physical values of the parameters when fitted to relevant experimental data. For example, τ_{cr} was predicted to be negative or extremely small ($\tau_{cr} \leqslant 0.05\sigma_Y$) in many cases, which is not possible; typically τ_{cr} is of the same order as σ_Y (here σ_Y is the yield stress). Further, a_1 was predicted to be negative in certain cases. As explained in Lim et al. (2013), a_1, accounting for the twinning-antitwinning asymmetry (Christian, 1983; Gröger et al., 2008a, 2008b), should be non-negative in order to account for higher resolved shear stress along the antitwinning direction. To avoid these anomalies, we determine a_1 separately by the procedure described below, and then solve for the rest of the parameters, a_2, a_3, and τ_{cr}, simultaneously.

Given the threefold symmetry of a ½ ⟨1 1 1⟩ screw dislocation in the bcc crystal (cf. Gröger et al. (2008a) and references therein), orientation dependence of the yield stress about ±30° of one reference slip plane of the {1 1 0} family is sufficient to determine the non-Schmid coefficients and may be applied to all slip planes. Note that ±30° correspond to the two {1 1 2} planes adjacent to a {1 1 0} plane along which twinning-antitwinning asymmetry is observed.

The parameter a_1 in Eq. (2) may be estimated by fitting the yield stress, σ_Y, on the maximum resolved shear stress plane (MRSSP) measured as a function of the angle, χ, which the MRSSP makes with the reference (1 1 0) slip plane about which the orientation dependence is measured (cf. (Chaussidon et al., 2006; Gröger et al., 2008b; Vitek et al., 2004a)). This may be mathematically expressed as (Chaussidon et al., 2006; Vitek et al., 2004a)

$$\sigma_Y = \frac{\sigma^0}{\cos\chi + a_1\cos(\chi + \pi/3)} \tag{3}$$

where σ^0 is a material constant. Note that this expression is a simplified form of Eq. (2) obtained by combining τ_{cr}, and the a_2 and a_3 terms into σ^0. Transformation of the yield rule from the slip system tensorial description in Eq. (2) to the angular (i.e., χ) dependence in Eq. (3) is a consequence of the bcc crystal symmetry and definition of the slip systems and corresponding non-Schmid slip planes (Gröger et al., 2008b).
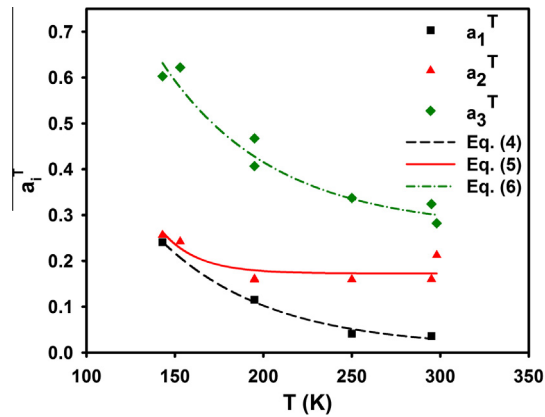
Spitzig and Keh (1970a) performed experimental studies on single crystal Fe to explore the temperature dependence of the proportional limit stress in uniaxial tension, σ_{pl}, as a function of χ about the (ī 0 1) slip plane. These values, extracted from Fig. 5 in Spitzig and Keh (1970a), are given in Table 1. Assuming $\sigma_Y \approx \sigma_{pl}$, a_1^T is estimated for different temperatures by fitting the experimental data in Table 1 to Eq. (3) using a least squares regression method, and is given in Table 1. The superscript T on a_1^T denotes the respective temperature. Based on the fit, a_1^T is found to decrease monotonically as the temperature is increased from 143 K to 295 K. Molecular statics simulations (Chaussidon et al., 2006; Koester et al., 2012) have estimated that $a_1^{0K} = 0.61$. From calculations, $a_1^{250K} \approx 0.07a_1^{0K}$ and $a_1^{295K} \approx 0.06a_1^{0K}$. This verifies that twinning-antitwinning asymmetry, though present, is significantly diminished at room temperature for Fe. Compiling the values of a_1^T estimated over different temperatures, the variation of a_1^T as a function of T is shown in Fig. 1. Least square fit of these data points to an exponential decay function is also shown in Fig. 1, and has the following form:

$$a_1^T = 0.0106 + 2.3311\exp(-0.0162T); 143\text{ K} \leqslant T \leqslant 298\text{ K} \tag{4}$$

Table 1
Least squares fit of non-Schmid coefficient, a_1, to the experimentally measured variation of σ_{pl} as a function of χ (from Spitzig and Keh (1970a)) for different temperatures using Eq. (3).

T(K)	χ(°)	$\sigma_{pl}/\sigma_{pl}(\chi = 0°)$	a_1^T	$\sigma^0/\sigma_{pl}(\chi = 0°)$
143	−24	1.02	0.2407	1.125
	0	1		
	10	1.05		
	20	1.15		
195	−24	1.04	0.1154	1.05
	0	1		
	10	1.03		
	20	1.08		
250	−24	1.08	0.0414	1.02
	0	1		
	10	1.03		
	20	1.05		
295	−24	1.08	0.0363	1.015
	0	1		
	10	1.02		
	20	1.04		

Fig. 1. Variation of non-Schmid coefficients with temperature.

Note that the value of $\sigma_{pl}/\sigma_{pl}(\chi = 0°)$ at $\chi = ±30°$ was also reported for all temperatures in Spitzig and Keh (1970a). However, these data points did not give good fit to Eq. (3) for $T = 143$ K and $T = 195$ K. Hence, these data points were excluded from the estimation of a_1^T for all temperatures. As mentioned earlier, Eqs. (2) and (3) give the orientation dependence of yield on non-Schmid stresses to a first order approximation; higher order stress terms may be needed for fitting the non-Schmid coefficients over the entire range (even at $\chi = ±30°$). Similar problems were also encountered when estimating a_1 from molecular statics results (cf. Chaussidon et al. (2006)).

Having determined a_1^T, we are now left with three parameters: τ_{cr}^T, a_2^T, a_3^T. Using the values of orientation-dependent yield stress, these parameters are estimated by solving a system of linear equations corresponding to different orientations for Eq. (2). Two sets of temperature-dependent non-Schmid parameters were obtained based on two different sets of experimental data for bcc-Fe (Spitzig and Keh, 1970a; Takeuchi, 1969). These values are reported in Table 2 and plotted as a function of temperature in Fig. 1. Note that the same value of a_1^T (from Eq. (4)) was used in both these calculations.

Table 2
Estimate of a_2^T and a_3^T by fitting orientation-dependent yield stress to Eq. (2) for different temperatures.

Experimental data	$\dot{\varepsilon}(s^{-1})$	T(K)	a_2^T	a_3^T	Stress measure
Spitzig and Keh (1970a)	5.6×10^{-4}	143	0.2564	0.6028	Proportional limit
		195	0.1590	0.4069	
		250	0.1595	0.3373	
		295	0.1601	0.3243	
Takeuchi (1969)	4.0×10^{-3}	153	0.2422	0.6222	Lower yield
		195	0.1609	0.4673	
		298	0.2124	0.2822	

Except for the value of a_2^T in the temperature range 295–298 K, the calculated values of a_2^T and a_3^T are comparable from both experimental data sets at similar temperatures, though the non-Schmid coefficients calculated from Takeuchi (1969) are generally higher than that calculated from Spitzig and Keh (1970a). This might be due to the fact that the lower yield stress was reported in Takeuchi (1969), while the proportional limit stress was reported in Spitzig and Keh (1970a). In terms of deformation, the point of proportional limit occurs prior to the lower yield point. Physically, the non-Schmid stresses are considered to assist in constricting the screw dislocation cores for glide to initiate (i.e., yield to occur) in bcc crystals. Full constriction of the dislocation cores might not have occurred at proportional limit, thus reflecting in slightly lower non-Schmid contributions as compared to that at the lower yield point.

It can be seen from Table 2 that both a_2^T and a_3^T decrease with increase in temperature, and start saturating in the range 250–298 K (similar to a_1^T). However, the contribution of these non-Schmid components to yield is still significant at room temperature, in contrast to the near-negligible contribution of the twinning-antitwinning asymmetry component. Temperature dependence of a_2^T and a_3^T, fit to exponential decay functions, are given in Eqs. (5) and (6), respectively.

$$a_2^T = 0.1727 + 108.9126 \exp(-0.0496T); \ 143 \text{ K} \leqslant T \leqslant 298 \text{ K} \tag{5}$$

$$a_3^T = 0.2699 + 3.5454 \exp(-0.0160T); 143 \text{ K} \leqslant T \leqslant 298 \text{ K} \tag{6}$$

From atomistic simulations (Koester et al., 2012), $a_2^{0K} = 0.23$ and $a_3^{0K} = 0.55$. These values are marginally lower than the calculated corresponding non-Schmid parameters at 143 K. Physically, these non-Schmid components represent the contribution of shear stresses perpendicular to the slip direction in constricting the distorted dislocation core (Gröger et al., 2008b). Calculated values of these coefficients from (isolated dislocation) atomistic simulations might have been lower because dislocation–dislocation interactions in distorting the core are not accounted for in the atomistic simulations. Unlike a_1^T, both a_2^T and a_3^T are not negligible at 250 K and 295 K. Physically, this means that resolved stresses normal to the Schmid and the 'non-glide' plane still contribute to the constriction of screw dislocation cores (for glide to initiate) at ambient temperatures.

Table 3 gives the relative contributions of the Schmid and non-Schmid stress components to the critical resolved shear stress, τ_{cr}^T, as a function of temperature. Approximate loading orientations were estimated from the stereographic projections given in Spitzig and Keh (1970a). All calculations were performed for slip system β with the highest Schmid factor, assuming single slip at yield. As can be seen, the relative non-Schmid stress contributions to τ_{cr}^T decrease markedly with increase in temperature. They are each less than 7% of τ_{cr}^T at 295 K; although diminished, non-Schmid effects are still present at room temperature. More importantly, the calculated value of τ_{cr}^T (sum of the Schmid and the non-Schmid stress components) for different orientations at a given temperature is more or less invariant (all values are within 4% of the mean τ_{cr}^T calculated at a given temperature). Physically, τ_{cr}^T denotes the resistance to dislocation glide at yield; τ_{cr}^T is a material property and should be the same irrespective of the loading orientation. In our calculations, τ_{cr}^T is a function of the yield stress and the non-Schmid coefficients. While the yield stress values are taken from experiments, the non-Schmid coefficients are estimated here. This verifies that the estimated coefficients, a_1^T, a_2^T, and a_3^T, are indeed addressing the experimentally observed temperature-dependent non-Schmid yield behavior.

Using atomistic simulations of a ½ ⟨1 1 1⟩ screw dislocation in bcc-Fe (Koester et al., 2012), the yield stress criterion given in Eq. (2) may be extended to directly account for the effect of tension/compression perpendicular to the glide direction and also to account for the fact that hydrostatic stress does not contribute to dislocation glide. This leads to three additional terms in the expression for the critical yield stress (Koester et al., 2012). For simplicity, the effect of these additional non-Schmid stresses on yield behavior is not considered the present work.

Table 3
Relative contributions of Schmid and non-Schmid stress components to τ_{cr}^T as a function of temperature.

T (K)	χ (°)	Loading orientation	σ_Y (MPa)	$\mathbf{m}^\beta \cdot \boldsymbol{\sigma} \cdot \mathbf{n}^\beta$ (MPa)	$a_1^T \mathbf{m}^\beta \cdot \boldsymbol{\sigma} \cdot \mathbf{n}_{ns}^\beta$ (MPa)	$a_2^T (\mathbf{n}^\beta \times \mathbf{m}^\beta) \cdot \boldsymbol{\sigma} \cdot \mathbf{n}^\beta$ (MPa)	$a_3^T (n_{ns}^\beta \times \mathbf{m}^\beta) \cdot \boldsymbol{\sigma} \cdot \mathbf{n}_{ns}^\beta$ (MPa)	τ_{cr}^T (MPa)
143	−24	[1 2 2 0]	234.09	104.05	21.45	−13.83	45.38	157.05
	0	[$\bar{1}$ 3 7]	229.5	114.34	13.75	0	33.94	162.03
	20	[$\bar{3}$ 7 9]	263.93	120.93	4.85	13.85	15.19	154.82
195	−24	[1 2 2 0]	131.56	58.48	5.49	−5.30	17.27	75.94
	0	[$\bar{1}$ 3 7]	126.5	63.02	3.45	0	12.67	79.14
	20	[$\bar{3}$ 7 9]	136.62	62.60	1.14	4.89	5.33	73.96
250	−24	[1 2 2 0]	58.10	25.83	1.13	−2.26	5.99	30.69
	0	[$\bar{1}$ 3 7]	53.8	26.80	0.69	0	4.23	31.72
	20	[$\bar{3}$ 7 9]	56.76	26.01	0.22	1.96	1.74	29.93
295	−24	[1 2 2 0]	32.51	14.45	0.37	−1.26	3.02	16.58
	0	[$\bar{1}$ 3 7]	30.10	14.99	0.23	0	2.12	17.34
	20	[$\bar{3}$ 7 9]	31.30	14.34	0.07	1.08	0.86	16.35

[a]Experimental uniaxial tension yield stress data from Spitzig and Keh (1970a).

4. Crystal plasticity framework

The finite deformation crystal plasticity model is based on the multiplicative deformation of the deformation gradient, $\boldsymbol{F}$, into elastic, $\boldsymbol{F}^e$, and inelastic, $\boldsymbol{F}^i$, parts (Asaro and Rice, 1977; Asaro, 1983). The inelastic velocity gradient, $\boldsymbol{L}^i$, given by $\boldsymbol{L}^i = \dot{\boldsymbol{F}}^i \cdot \boldsymbol{F}^{i-1}$, is the tensor sum of the crystallographic shearing rate, $\dot{\gamma}^\alpha$, over all slip systems, N_s, i.e.,

$$\boldsymbol{L}^i = \sum_{\alpha=1}^{N_s} \dot{\gamma}^\alpha \boldsymbol{m}_0^\alpha \otimes \boldsymbol{n}_0^\alpha \tag{7}$$

where $\boldsymbol{m}_0^\alpha$ and $\boldsymbol{n}_0^\alpha$ are unit vectors corresponding to the slip and slip plane normal directions in the reference (or intermediate) configuration. The shearing rate, $\dot{\gamma}^\alpha$, is a function of the resolved shear stress, τ^α, and the internal state variables (ISVs) on each slip system α. The slip system dislocation density, ρ^α, given as the additive sum of mobile, ρ_M^α, and immobile dislocations, ρ_I^α, i.e., $\rho^\alpha = \rho_M^\alpha + \rho_I^\alpha$, is used as an ISV in this framework.

4.1. Dislocation glide kinetics

Thermally activated glide of $\frac{1}{2} \langle 1\,1\,1 \rangle$ screw dislocations by kink-pair formation is the rate controlling mechanism governing inelastic deformation in bcc metals at low temperatures (cf. Argon (2008)). In continuum constitutive formulations, the crystallographic shearing rate due to thermally activated dislocation glide is generally represented using a phenomenological Kocks-type activation enthalpy driven flow rule (Kocks et al., 1975), i.e.,

$$\dot{\gamma}^\alpha = \begin{cases} \dot{\gamma}_0 \exp\left(-\frac{\Delta F_g}{kT}\left(1 - \left(\frac{\tau_f^\alpha - s_a^\alpha}{s_t^\alpha}\right)^p\right)^q\right); & \text{for } \tau_f^\alpha > s^\alpha \\ 0; & \text{for } \tau_f^\alpha \leqslant s^\alpha \end{cases} \tag{8}$$

where $\dot{\gamma}_0$ is the pre-exponential factor, ΔF_g is the activation energy for dislocation glide in the absence of external stress, k is Boltzmann constant, T is absolute temperature, τ_f^α is the driving stress for dislocation glide, s_a^α is the athermal slip resistance to dislocation glide, s_t^α is the thermal resistance, typically governed by the high Peierls stress in bcc metals, and p and q are parameters used to model the shape of the activation enthalpy function. Note that the kink-pair mechanism in bcc metals is governed by two different temperature regimes (cf. Argon (2008)). For simplicity, these two regimes are not considered explicitly in the present work.

The purpose of this work is to demonstrate a top-down approach for modeling non-Schmid effects in bcc metals at finite temperatures. It should be noted that while the coarse-grained constitutive models developed/used in this work are phenomenological in nature, we still consider the screw dislocation movement by kink-pair formation as the rate-controlling mechanism. In more (atomistically-derived) physical formulations, the crystallographic shearing rate is generally expressed as (Narayanan et al., 2014)

$$\dot{\gamma}^\alpha = \dot{\gamma}_0 \exp\left(-\frac{H_{\text{kp}}(\tau_f^\alpha, T)}{kT}\right) \tag{9}$$

where $H_{\text{kp}}(\tau_f^\alpha, T)$ is the stress- and temperature-dependent activation free energy of kink-pair formation. In a recent study (Narayanan et al., 2014), the nudged elastic band method has been used to calculate the kink-pair formation energy from the approximate 0 K potential energy landscape (i.e., $H_{\text{kp}}(\tau_f^\alpha, T) \approx H_{\text{kp}}(\tau_f^\alpha, T = 0)$). However, to fully account for the effect of activation entropy and the associated Meyer-Neldel compensation rule (Zhu et al., 2013), one should calculate the activation *free energy* (as opposed to 0 K potential energy) as a function of all the stress components at various temperatures. At the moment, this is a very difficult task from the atomistic modeling standpoint. Hence, the present work represents an empirical characterization of temperature effects on the activation free energy of kink-pair formation in terms of the temperature-dependent parameters, a_1, a_2, and a_3. The functional form for $H_{\text{kp}}(\tau_f^\alpha, T)$ given in Eq. (8) is simple enough for the parameters to be estimated directly from available experimental data. As will be shown later, this Kocks-type flow rule replicates the inelastic flow response fairly well.

The long range athermal slip resistance, s_a^α, due to dislocation–dislocation interactions, may be expressed as a function of the dislocation density using a Taylor hardening model, i.e.,

$$s_a^\alpha = Gb\sqrt{\sum_{\zeta=1}^{N_s} q_\rho A^{\alpha\zeta} \rho^\zeta} \tag{10}$$

where G is the shear modulus, b is the Burgers vector magnitude, q^ρ is the dislocation barrier strength, and, $A^{\alpha\zeta}$ is the matrix of slip system dislocation interaction coefficients.

Strictly speaking, the driving stress for dislocation glide, τ_f^α, is just the resolved shear stress, τ^α, on slip system α; this must hold whether yield (i.e., initiation of glide at a threshold) follows Schmid's law or not. However, crystal viscoplastic formulations do not generally model yield and inelastic flow separately. Yield is implicitly modeled in the flow rule using the lattice resistance or a similar threshold-like term.

In the present formulation, we assume the initial (threshold) driving stress to be the additive sum of the resolved shear stress, τ^α, and the contribution from non-Schmid stresses, σ_{ns}^α, i.e.,

$$\tau_f^\alpha\big|_{initial} = \tau^\alpha + \sigma_{ns}^\alpha \tag{11}$$

From Eq. (2), σ_{ns}^α has the following form:

$$\sigma_{ns}^\alpha = a_1^T \boldsymbol{m}^\alpha \cdot \boldsymbol{\sigma} \cdot \boldsymbol{n}_{ns}^\alpha + a_2^T (\boldsymbol{n}^\alpha \times \boldsymbol{m}^\alpha) \cdot \boldsymbol{\sigma} \cdot \boldsymbol{n}^\alpha + a_3^T (\boldsymbol{n}_{ns}^\alpha \times \boldsymbol{m}^\alpha) \cdot \boldsymbol{\sigma} \cdot \boldsymbol{n}_{ns}^\alpha \tag{12}$$

Eq. (11) thus satisfies the yield relation given in Eq. (2). However, in view of the foregoing statement that resolved shear stress drives dislocation glide, Eq. (11) should be modified beyond the point of yield such that the contribution from non-Schmid stresses diminishes with inelastic deformation. From a physical standpoint, it is unlikely that the non-Schmid effects would suddenly disappear; not all dislocations start gliding at the point of initial yield, meaning that not all dislocation cores get constricted simultaneously at yield. The core structure is also expected to change with the nucleation of double kinks during dislocation glide. Further, long range interaction fields with other dislocations may be expected to affect the extent of dislocation core constriction. In order to model these effects, we propose to model this decay of the non-Schmid contribution to the driving stress as an exponential function of the effective inelastic strain, ε_{eff}^i, i.e.,

$$
\begin{aligned}
\tau_f^\alpha &= \tau^\alpha + a_1^T \exp\left(-\frac{\varepsilon_{eff}^i}{\varepsilon_0^i}\right) \boldsymbol{m}^\alpha \cdot \boldsymbol{\sigma} \cdot \boldsymbol{n}_{ns}^\alpha + a_2^T \exp\left(-\frac{\varepsilon_{eff}^i}{\varepsilon_0^i}\right) (\boldsymbol{n}^\alpha \times \boldsymbol{m}^\alpha) \cdot \boldsymbol{\sigma} \cdot \boldsymbol{n}^\alpha + a_3^T \exp\left(-\frac{\varepsilon_{eff}^i}{\varepsilon_0^i}\right) (\boldsymbol{n}_{ns}^\alpha \times \boldsymbol{m}^\alpha) \cdot \boldsymbol{\sigma} \cdot \boldsymbol{n}_{ns}^\alpha \\
&= \tau^\alpha + \sigma_{ns}^\alpha \exp\left(-\frac{\varepsilon_{eff}^i}{\varepsilon_0^i}\right)
\end{aligned} \tag{13}
$$

where ε_0^i is the decay constant representing the effective inelastic strain at which the contribution of the non-Schmid stresses to the driving stress reduces to about 37% of their initial contribution at yield. As the contribution of non-Schmid stresses decays with increasing inelastic strain, the resolved shear stress, τ^α, dominates the driving force for dislocation glide. A parametric study of this constitutive model, along with comparison to the experimental data, is presented in Section 6.3.

Note that the non-Schmid stresses may be assumed to decay as a function of the dislocation density, ρ^α, or some other state variable. For simplicity we choose the constitutive form given in Eq. (13). Detailed experimental studies, for example, of the orientation dependence of yield in pre-strained single crystals, are needed to determine the exact nature of the decay of non-Schmid effects with applied strain; the constitutive model may be modified accordingly from its present exponential decay form.

4.2. Dislocation evolution

The authors have earlier developed constitutive equations for the evolution of mobile and immobile dislocations in bcc metals subjected to radiation damage (Patra and McDowell, 2012). Neglecting terms representing the interaction of dislocations with irradiation-induced defects, the rate of evolution of mobile and immobile dislocations, as a function of the crystallographic shearing rate, $\dot{\gamma}^\alpha$, is given as (Patra and McDowell, 2012)

$$\dot{\rho}_M^\alpha = \frac{k_{mul}}{b}\sqrt{\sum_\varsigma \rho^\varsigma}|\dot{\gamma}^\alpha| - k_{cs}\exp\left(-\frac{(\tau^* - |\tau^\chi|)V_a}{kT}\right)\rho_M^\alpha|\dot{\gamma}^\alpha| - \frac{2R_c}{b}\rho_M^\alpha|\dot{\gamma}^\alpha| - \frac{1}{b\lambda^\alpha}|\dot{\gamma}^\alpha| \tag{14}$$

$$\dot{\rho}_I^\alpha = \frac{1}{b\lambda^\alpha}|\dot{\gamma}^\alpha| - k_{dyn}\rho_I^\alpha|\dot{\gamma}^\alpha| \tag{15}$$

The first term in Eq. (14) represents the rate of formation of new mobile dislocations by multiplication at existing dislocation segments, the second term represents the rate of migration of mobile dislocations by cross-slip (from slip plane α to slip plane χ), the third term represents the rate of mutual annihilation of mobile dislocation segments with opposite Burgers vectors within a critical capture radius R_c, and the fourth term represents the rate of immobilization of mobile dislocation segments by trapping at barriers, given as a function of the effective mean free path, $\lambda^\alpha = 1/\beta_\rho\sqrt{\rho^\alpha}$, of the glide dislocations. The corresponding rate of addition of immobile dislocations due to trapping of mobile dislocations is reflected in the first term of Eq. (15), while the second term represents the rate of annihilation of immobile dislocations by dynamic recovery. In these equations, k_{mul}, k_{cs}, and k_{dyn} are material constants corresponding to mobile dislocation multiplication, mobile dislocation cross-slip, and dynamic recovery of immobile dislocations, respectively. τ^* is the activation stress for cross-slip over an activation volume, V_a, and β_ρ is a constant associated with dislocation trapping. These equations are assumed to principally reflect the dislocation mechanisms governing inelastic deformation in bcc-Fe. Patra and McDowell (2012) provide a detailed description of the physical mechanisms modeled and the assumptions involved.

5. Model parameters

Temperature dependent elastic constants for bcc-Fe are adopted from Adams et al. (2006). As mentioned earlier, the material is assumed to have 24 {110} ⟨111⟩ slip systems, considering both positive and negative slip. These slip systems are listed in Gröger et al. (2008b). Based on bcc crystallography, the Burgers vector magnitude of Fe is given as $b = (\sqrt{3}/2)a_0$, where $a_0 = 0.2866$ nm is the lattice parameter of bcc-Fe (Johnson and Oh, 1989).

The zero-stress activation energy for dislocation glide, ΔF_g, shape function parameters, p and q, and the pre-exponential factor in the flow rule, $\dot{\gamma}_0$, were used for fitting the simulated orientation- and temperature-dependent yield stress and the initial hardening response to experiments. Based on the fit (discussed in Section 6), $\Delta F_g = 0.825$ eV, $p = 0.47$, $q = 1.0$, and $\dot{\gamma}_0 = 1.0 \times 10^7 \text{ s}^{-1}$. Note that our value of activation energy, ΔF_g, is in the range predicted by experiments, ~ 0.65–0.9 eV (Brunner and Diehl, 1991a, 1991b, 1991c; Spitzig and Keh, 1970b).

Temperature dependence of the non-Schmid coefficients, a_1^T, a_2^T and a_3^T, was discussed in Section 3. The non-Schmid contribution to the driving stress has been modeled to decay as an exponential function of the effective inelastic strain, ε_{eff}^i, in Eq. (13). The value of the associated material constant, ε_0^i, is assumed to be 0.02, meaning that the non-Schmid contribution at $\varepsilon_{eff}^i = 0.02$ decreases to $\sim 37\%$ of the contribution at initial yield ($\varepsilon_{eff}^i = 0$). Systematic experiments/atomistic simulations are needed to further refine this phenomenological relation. Parametric study of the effect of ε_0^i on the simulated stress–strain curves is shown in Section 6.3.

From Suzuki et al. (1995), the thermal lattice resistance, s_t^α, essentially the intrinsic Peierls stress, is $s_t^\alpha = 390$ MPa. The dislocation barrier strength, q^ρ, is assumed to be 0.3 in the expression for s_a^α. A similar value was used in Arsenlis et al. (2004) to model the dislocation barrier resistance in irradiated Cu. The values of the dislocation interaction coefficients were assumed to be $A^{\alpha\alpha} = 1.0$ (self-interaction) and $A^{\alpha\varsigma}(\varsigma \neq \alpha) = 0.2$ (latent interaction). From experiments (Spitzig and Keh, 1970b, 1970c), $s_a^\alpha \approx 5$–8 MPa at initial yield. Putting in values of the above mentioned parameters in Eq. (10), the initial value of dislocation density, $\rho^0 \approx 4.0 - 10.0 \times 10^4 \text{ mm}^{-2}$. This value of dislocation density is within the limits of that estimated by Keh (1965) for Fe single crystals without significant inelastic deformation. There are no relevant experimental data to indicate the fraction of this dislocation density that is immobile in nature. We assume that an equal population of mobile and immobile dislocations exists initially as representative of the remnant deformation history, if any, prior to recrystallization (cf. Keh (1965) for a description of the growth of Fe single crystals from polycrystalline bars). Accordingly, an initial dislocation density of $\rho_M^0 = \rho_I^0 = 4.0 \times 10^4 \text{ mm}^{-2}$ is assigned on all slip systems. A similar assumption of equal initial population of mobile and immobile dislocations has also been made by Li et al. (2014) for single crystal Fe.

Parameters associated with the dislocation evolution equations include: k_{mul}, k_{cs}, k_{dyn}, τ^*, V_a, R_c, and β_ρ. Since this work focuses on modeling the mechanical behavior of bcc-Fe at low and ambient temperatures, dislocation migration due to thermally activated cross-slip may be neglected at these temperatures, i.e., $k_{cs} = 0$ (see Patra and McDowell (2012) for values of the parameters, τ^* and V_a, when k_{cs} is non-zero). The critical capture radius, R_c, for mutual annihilation of dislocation dipoles is assumed to be $6b$ (≈ 1.5 nm). This is of the same order as that used in Arsenlis et al. (2004) for mutual dislocation dipole annihilation in irradiated Cu. The remaining parameters, k_{mul}, k_{dyn}, and β_ρ, were used to fit simulation results to the experimental single crystal stress–strain curves of bcc-Fe (Keh, 1965) for different loading orientations at 298 K. Based on the fit (shown in Section 6.1), $k_{mul} = 3.45 \times 10^{-2}$, $k_{dyn} = 2.75 \times 10^2$, and $\beta_\rho = 7.40 \times 10^{-2}$. These parameters are assumed to be temperature invariant. Table 4 lists the values of the complete set of parameters.

Table 4
Model parameters for bcc-Fe.

Parameter	Value	Meaning
C_{11}, C_{12}, C_{44}, v	$239260 - 24520/(\exp(392.03/T[\text{K}]) - 1)$ MPa, $135780 - 6550/(\exp(469.65/T[\text{K}]) - 1)$ MPa, $120720 - 3500/(\exp(162.9/T[\text{K}]) - 1)$ MPa, 0.29	Elastic constants (from Adams et al. (2006))
G	$87600 - 17T[\text{K}]$ MPa	Shear modulus (from Naamane et al. (2010))
a_0	0.2866 nm	Lattice parameter (from Johnson and Oh (1989))
ΔF_g, p, q, $\dot{\gamma}_0$	0.825 eV, 0.47, 1.0, $1.0 \times 10^7 s^{-1}$	Flow rule parameters
a_1^T, a_2^T, a_3^T	$a_1^T = 0.0106 + 2.3311\exp(-0.0162T)$; $143\text{ K} \leqslant T \leqslant 298\text{ K}$, $a_2^T = 0.1727 + 108.9126\exp(-0.0496T)$; $143\text{ K} \leqslant T \leqslant 298\text{ K}$, $a_3^T = 0.2699 + 3.5454\exp(-0.0160T)$; $143\text{ K} \leqslant T \leqslant 298\text{ K}$	Non-Schmid parameters
q^ρ, $A^{\alpha\alpha}$, $A^{\alpha\varsigma}(\varsigma \neq \alpha)$, s_t^α	0.3, 1.0, 0.2, 390 MPa	Hardening parameters
ε_0^i	0.02	Parameter for decay of non-Schmid stresses
k_{mul}, k_{cs}, k_{dyn}, R_c, β_ρ	3.45×10^{-2}, 0, 2.75×10^2, $6b$, 7.40×10^{-2}	Dislocation evolution parameters

6. Model results and discussion

6.1. Orientation-dependent stress–strain curves at 298 K

The constitutive model was implemented in the finite element program ABAQUS (2007) using the User MATerial (UMAT) subroutine. Three-dimensional displacement-controlled simulations were performed on a cubic simulation cell of size 100 μm on each side. Periodic boundary conditions were imposed in all directions, implying that the displacements on opposite boundaries are tied to each other. As described in van der Sluis et al. (2000), the displacements on each boundary are also tied to that on reference node (on which the net prescribed displacement is imposed). The simulation cell was loaded uniaxially (in tension or compression) at a strain rate of $10^{-4}\,s^{-1}$, with sides free of net traction. The same crystallographic orientation, representative of the single crystal, was assigned to all elements in the simulation cell.

The constitutive model was fit to the experimental initial hardening response (up to ≈5% strain) of single crystal Fe loaded in three different orientations, [0 0 1], [0 1 1] and [$\bar{1}$ 1 1], at 298 K. Fig. 2 compares the simulated stress–strain curves with the experimental data (Keh, 1965; Yalcinkaya et al., 2008). A reasonable fit was obtained for the stress–strain response in all three orientations. However, the simulated yield stress for the [$\bar{1}$ 1 1] orientation was slightly lower than the experimentally measured value. The simulated initial work hardening rate for the [$\bar{1}$ 1 1] orientation was higher than that measured in experiments until it approaches the experimentally observed hardening rates at ∼0.01 true strain. Note that the non-Schmid parameters were calculated from a different set of experiments (Spitzig and Keh, 1970a; Takeuchi, 1969). Small differences in material composition might have resulted in different values of yield stress. For example, it has been shown (Stein and Low, 1966) that ppm level carbon concentration difference can result in non-negligible difference in the yield stress of Fe single crystals, especially at low temperatures. If the experimental data from Keh (1965) were used for calculating the non-Schmid parameters, $a_1^{298K} = 0.0363$, $a_2^{298K} = -0.0333$, $a_3^{298K} = 0.1417$, and $\tau_{cr}^{298K} = 17.87$ MPa. Due to lack of systematic data regarding the variation of orientation-dependent yield stress with temperature in Keh (1965), these experimental results were not used to estimate the non-Schmid parameters. Nevertheless, the overall stress–strain response of the simulated material is in qualitative agreement with experiments.

Fig. 3 shows the evolution of average mobile and immobile dislocation densities as a function of strain for the three loading orientations. These dislocation densities are averaged over all slip systems. While the dislocation densities (both mobile and immobile components) saturate for the [0 1 1] loading case, this is not the case for [0 0 1] and [$\bar{1}$ 1 1] loading. The hardening behavior in the stress–strain curves in Fig. 2 suggests the same (athermal hardening is a function of dislocation density). Further, the mobile dislocation density for the [0 0 1] and [$\bar{1}$ 1 1] loading cases increases asymptotically. This dislocation evolution behavior is qualitatively similar to that seen in experiments (Keh, 1965); the nature of dislocation evolution, asymptotic or saturating, is a function of the loading orientation and active slip systems.

6.2. Temperature dependent yield stress

The constitutive equations were used to predict the yield stress of single crystal Fe for various temperatures and loading orientations. The model predictions were compared to the experimental data (Spitzig and Keh, 1970a) for the material loaded in [1 1 1 6], [$\bar{1}$ 3 7], and [$\bar{4}$ 9 9] orientations at 143 K, 195 K, 250 K, and 295 K. Fig. 4 compares the yield stress measured from simulations to the corresponding experimental data as a function of angle, χ, which the MRSSP makes with the reference (1 1 0) slip plane. Angles $\chi = -30°$, $\chi = 0°$, and $\chi = 30°$ in Spitzig and Keh (1970a) roughly correspond to the [1 1 1 6],
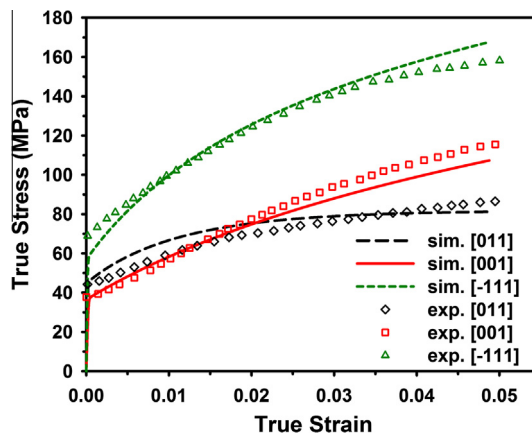

Fig. 2. Comparison of simulations (solid and dotted lines) calibrated to the experimental stress–strain curves (open symbols) for three different orientations at 298*K*. Experimental data from Keh (1965).
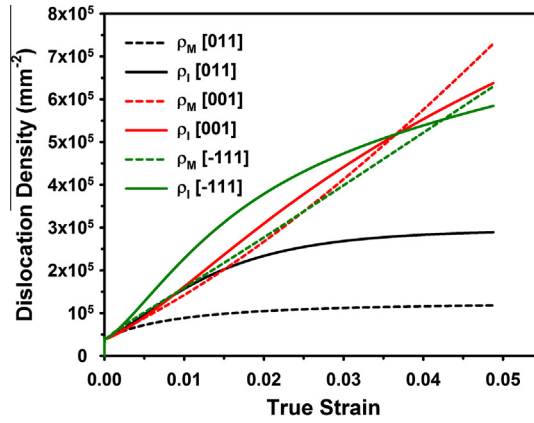
Fig. 3. Evolution of the average dislocation density as a function of strain for different orientations.
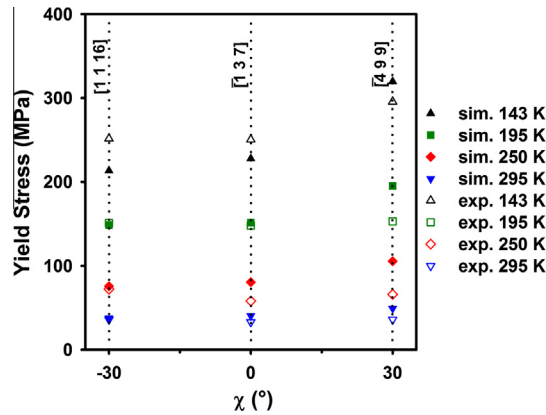

Fig. 4. Comparison of yield stress from simulations (closed symbols) with experiments (open symbols) for different loading orientations and temperatures.

$[\bar{1}37]$, and $[\bar{4}99]$ loading orientations, respectively. Except for the $[\bar{4}99]$ loading, the predicted orientation-dependent yield behavior was comparable to experiments, though slightly under-predicted at 143 K. The yield stress for $[\bar{4}99]$ orientation was over-predicted at all temperatures. As mentioned earlier in Section 3, the experimental yield stress for this orientation, $\chi = 30°$, was not used to estimate the non-Schmid coefficients; a higher order stress term may be necessary to capture the yield behavior for this orientation. Generally, this orientation is also excluded in estimation of non-Schmid parameters from atomistic simulations (cf. Chaussidon et al. (2006)).

Yield stress, in the present case, is a function of the non-Schmid stresses, as well as the slip resistance. Of these, the non-Schmid stresses are orientation and temperature dependent (Eqs. (4)–(6)). Temperature dependence of the slip resistance was not considered in the present work; the simulated hardening response lacks agreement in many cases with the experimental hardening response at lower temperatures. Moreover, the hardening response was calibrated using a different set of experiments (Keh, 1965) at 298 K. It may be expected that the simulated hardening will not fit the experimental results from Spitzig and Keh (1970a) at lower temperatures.

A ratio of the total resolved stress, including non-Schmid terms, to the Schmid stress (on slip system β with the highest Schmid factor) is defined as

$$R_{ns}^{T} = \frac{\boldsymbol{m}^{\beta} \cdot \boldsymbol{\sigma} \cdot \boldsymbol{n}^{\beta} + a_{1}^{T} \boldsymbol{m}^{\beta} \cdot \boldsymbol{\sigma} \cdot \boldsymbol{n}_{ns}^{\beta} + a_{2}^{T}(\boldsymbol{n}^{\beta} \times \boldsymbol{m}^{\beta}) \cdot \boldsymbol{\sigma} \cdot \boldsymbol{n}^{\beta} + a_{3}^{T}(\boldsymbol{n}_{ns}^{\beta} \times \boldsymbol{m}^{\beta}) \cdot \boldsymbol{\sigma} \cdot \boldsymbol{n}_{ns}^{\beta}}{\boldsymbol{m}^{\beta} \cdot \boldsymbol{\sigma} \cdot \boldsymbol{n}^{\beta}} \tag{16}$$

This ratio may be used for estimating the deviation from 'conventional' Schmid behavior at temperature T. Ratio R_{ns}^{T} is plotted for different temperatures in the standard stereographic triangle in Fig. 5(a)–(d). These values are calculated at the point of initial yield. The corresponding Schmid factor is plotted in Fig. 5(e). The deviation from Schmid behavior increases with decrease in temperature. The value of R_{ns}^{T}, although relatively lower, is slightly greater than unity at 250 K and 295 K. This suggests that non-Schmid effects are non-negligible at room temperature. Furthermore, R_{ns}^{T} is higher for crystallographic orientations between the $[001]$ and $[\bar{1}11]$ poles in the stereographic triangle. As one approaches the $[011]$ pole, R_{ns}^{T} decreases gradually to unity at all temperatures.
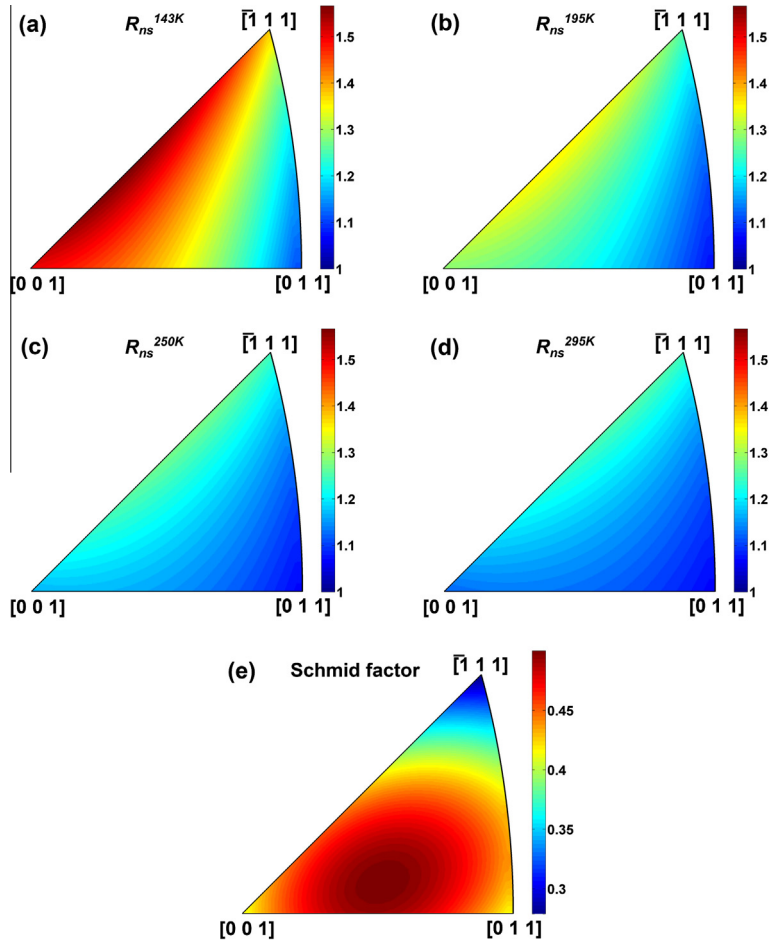
Fig. 5. (a–d): R_{ns}^T for uniaxial tension plotted in the stereographic triangle at 143 K, 195 K, 250 K, and 295 K, respectively; (e): Schmid factor for bcc metals assuming slip along the {1 1 0} planes.

6.3. Parametric study of ε_0^i

We proposed a constitutive model for the decay of non-Schmid effects as a function of the effective inelastic strain in Eq. (13). The behavior of this model is studied here as a function of the parameter, ε_0^i, that denotes the decay constant for the exponential decay of non-Schmid stresses. The effect of ε_0^i on the mechanical response of the specimen loaded in the [1 1 1 6] orientation was explored at 195 K. The stress–strain response without non-Schmid effects, i.e., associative flow was also simulated. Fig. 6 shows the stress–strain curves for all these cases compared to the experimental data. The 'associative' legend represents no non-Schmid effects, i.e., associative flow, and the open symbols show the experimental stress–strain curve from Spitzig and Keh (1970a) for the [1 1 1 6] loading at 195 K.

As ε_0^i is increased from 0.005 to 0.05, the initial flow stress decreases monotonically. The initial flow stress of the associative flow case is higher than those with non-Schmid stresses. Note that relaxation of the stress–strain response to a quasi-equilibrium state is observed at higher applied strains; this is more prominent for the material with lower ε_0^i. It might seem counter-intuitive that the material with higher non-Schmid stresses has a lower initial flow stress. Note that for glide to occur, the driving stress, τ_f^α, must overcome the lattice resistance. τ_f^α has contributions from the resolved shear stress, τ^α, and the non-Schmid stresses (both components of the macroscopic stress state). When non-Schmid stresses are present, they complement τ^α in overcoming the lattice resistance. However, for the case of associative flow, τ^α must have a higher relative contribution to τ_f^α; τ^α, and hence the macroscopic stress, has to increase to overcome the lattice resistance initially.

Comparison to experiments (Spitzig and Keh, 1970a) shows that the material with $\varepsilon_0^i = 0.02$ best fits the experimental stress–strain data, all other parameters unchanged. Accordingly, we have used $\varepsilon_0^i = 0.02$ in all our simulations. Systematic experiments, for example, uniaxial loading of crystals with different levels of pre-strain, are needed for a more rigorous validation of this constitutive model (higher pre-strain would relate to lower contribution of non-Schmid effects).
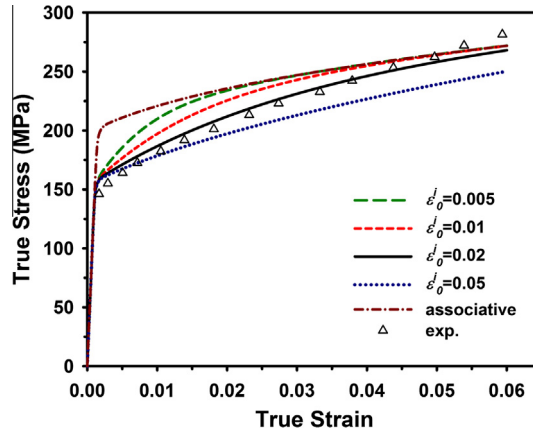
Fig. 6. Parametric effect of $\dot{\varepsilon}_0^i$ on the true stress–strain response of the material loaded in [1 1 1 6] orientation at 195 K compared to the associative flow behavior. Open symbols show the corresponding experimental data from Spitzig and Keh (1970a).

6.4. Tension–compression asymmetry

The constitutive model was used to predict the tension–compression (TC) asymmetry of single crystal Fe loaded in different orientations. This asymmetry is measured in terms of the strength differential, SD, given by (Bassani and Racherla, 2011)

$$SD = \frac{(\sigma_Y^t - \sigma_Y^c)}{(\sigma_Y^t + \sigma_Y^c)/2} \tag{17}$$

where, σ_Y^t is the yield stress in tension, and σ_Y^c is the yield stress in compression. Fig. 7 shows the variation of SD with temperature for various loading orientations. A negative value of SD indicates higher yield stress in compression.

As can be seen, the tension–compression asymmetry is highly orientation- and temperature-dependent. Loading orientations [0 0 1] and [1 1 1 6] are stereographically close by, hence the apparent overlap in their TC asymmetry behavior. The yield stress is generally higher in compression, except for the [0 1 1] orientation at 143 K. Similar predictions were also made for the TC asymmetry of single crystal Mo near the [0 1 1] pole by Lim et al. (2013) using a constitutive model with non-Schmid considerations. Except for the [0 1 1] orientation, the (magnitude of) TC asymmetry generally decreases with increase in temperature. While TC asymmetry is generally lower at 250 K and 295 K, it is still present at room temperature. It is not evident why the temperature dependence of TC asymmetry for the [0 1 1] orientation is qualitatively unlike that of the other loading orientations in Fig. 7. A higher yield stress in tension near the [0 1 1] pole was also observed in the atomistic studies of bcc-Mo at 0 K (Gröger et al., 2008b). The same atomistic study found, however, that the yield stress is always higher in compression for bcc-W at 0 K (Gröger et al., 2008b). These observations indicate that the nature of TC asymmetry varies for each bcc metal. Further, analytical calculations (Gröger et al., 2008b) suggest that the shear stresses perpendicular to the slip direction play a major role in TC asymmetry. Based on the limited orientations that we have considered in this work, it seems apparent that the [0 1 1] and [$\bar{1}$ 1 1] loading orientations serve as the upper and lower bounds, respectively, for the SD of bcc-Fe within the standard stereographic triangle.
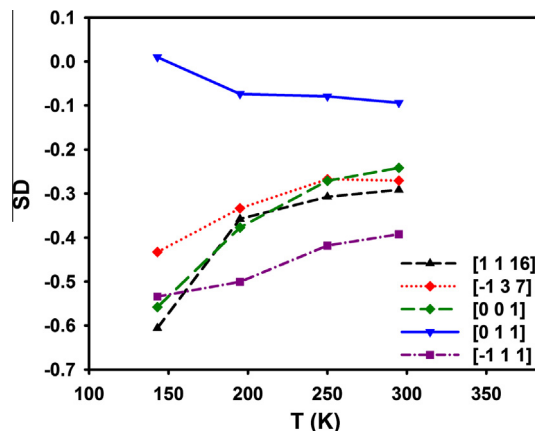

Fig. 7. Variation of the strength differential, SD, with temperature for different loading orientations.

This asymmetry arises from activation of different slip systems in tension and compression. A comparison of the possible activated slip systems in tension versus compression is given in Weinberger et al. (2012) for different loading orientations. At present, there is no systematic experimental data available to compare to our model predictions. However, experiments (Šesták and Zárubová, 1965; Takeuchi et al., 1967) have shown that TC asymmetry is indeed prevalent in similar Fe-Si alloys. Coupled experiments and modeling over different temperatures and loading orientations are needed to further understand this behavior.

7. Conclusions

Crystal plasticity constitutive equations have been developed for modeling orientation dependence and tension–compression asymmetry of single crystal bcc-Fe at low and ambient temperatures by attributing these effects to non-Schmid stresses that have been shown in previous 2D atomistic simulations to correlate with the non-planar screw dislocation core structure. Constitutive equations are also introduced for the decay of the non-Schmid contribution to the driving stress as a function of inelastic strain. These non-Schmid contributions are coupled with an existing dislocation density crystal plasticity framework to simulate the mechanical behavior of single crystal Fe. The model is fit to the experimental hardening response at 298 K. The yield stress and tension–compression asymmetry for different loading orientations and temperatures is also modeled. Model predictions are compared to available experimental data.

Temperature dependence of the non-Schmid parameters has not been examined previously, and is a unique contribution of the present work. Furthermore, previous continuum constitutive models generally use the non-Schmid parameters measured from atomistic simulations at 0 K. This might not be physically accurate, as experiments suggest that the non-Schmid effects decay with increase in temperature. In this work, the non-Schmid parameters and their temperature dependence are inferred entirely from available experimental data for Fe. The methodology adopted in this work may also be used to estimate the temperature dependence of non-Schmid parameters for other bcc metals, such as Mo and Ta.

While this work focused on the temperature dependence of non-Schmid effects, physical mechanisms behind these experimentally observed phenomena were not considered explicitly. Physically, the decay of non-Schmid effects may be linked to the transformation in deformation mechanism from the high stress, low temperature regime of dislocation bow out (Dorn and Rajnak, 1964) to the low stress, high temperature regime of 'well-developed' kinks. As explained in Gröger and Vitek (2008), twinning-antitwinning asymmetry and tension–compression asymmetry are expected to be less dominant in the low stress, high temperature regime. In our work, the flow rule representing kink-pair formation (Eq. (8)) did not consider these two mechanisms separately. Rather, a phenomenological activation enthalpy-driven flow rule was assumed for both regimes with a single set of parameters. Future work may model these two regimes explicitly.

This work employs a dislocation density-based approach for crystal plasticity modeling of temperature-dependent non-Schmid yield behavior in bcc metals, and relies on top-down experiments for parameter estimation. While a bottom-up approach employing atomistics (for example, Chen (2013)) may be provide a more intimate physical basis with regard to dislocation line level processes involved in kink-pair formation, such an approach is presently of largely qualitative character and can predict significantly higher Peierls stress values than seen in experiments. Moreover, many body dislocation interactions are difficult to consider in atomistic modeling. The top-down approach taken here can be used to model mesoscopic (polycrystal) and macroscopic deformation behavior in applications. Further calculations are needed to model the rate dependence on initial yield and inelastic flow, considering the effect of applied deformation rate on cooperative dislocation glide via kink-pair formation.

It will clearly take more time and effort to rectify and fully understand the applicability of the kind of non-Schmid type formulation of crystal plasticity pursued here relative to approaches that consider in more detail the processes of kink-pair formation at lower stress levels and finite temperatures representative of thermally activated flow in bcc crystals. The latter approaches do not resort to the non-planar dislocation core argument and associated non-Schmid stress effects in Eq. (2) (i.e., $a_1 = a_2 = a_3 = 0$) (Narayanan et al., 2014). However, tension–compression asymmetry is a challenge to be resolved in models that do not incorporate non-Schmid stresses. Ultimately, it is likely necessary to rectify and adopt combined bottom-up and top-down modeling approaches to address the complexity of screw/edge dislocation activities in bcc crystals to make connections between the multiscale hierarchy of atomistics, discrete dislocation dynamics, and crystal plasticity.

References

ABAQUS, 2007. Simulia. Dassault Systemes, Providence, RI.
Adams, J.J., Agosta, D.S., Leisure, R.G., Ledbetter, H., 2006. Elastic constants of monocrystal iron from 3 to 500 K. J. Appl. Phys. 100, 113530.
Argon, A.S., 2008. Strengthening Mechanisms in Crystal Plasticity. Oxford University Press, Oxford.
Arsenlis, A., Wirth, B.D., Rhee, M., 2004. Dislocation density-based constitutive model for the mechanical behaviour of irradiated Cu. Philos. Mag. 84, 3617–3635.

Asaro, R.J., 1983. Micromechanics of crystals and polycrystals. Adv. Appl. Mech. 23, 1–115.

Asaro, R.J., Rice, J.R., 1977. Strain localization in ductile single crystals. J. Mech. Phys. Solids 25, 309–338.

Bassani, J.L., Racherla, V., 2011. From non-planar dislocation cores to non-associated plasticity and strain bursts. Prog. Mater Sci. 56, 852–863.

Bassani, J.L., Ito, K., Vitek, V., 2001. Complex macroscopic plastic flow arising from non-planar dislocation core structures. Mater. Sci. Eng., A 319–321, 97–101.

Bolton, C.J., Taylor, G., 1972. Anomalous slip in high-purity niobium single crystals deformed at 77°K in tension. Philos. Mag. 26, 1359–1376.

Brunner, D., Diehl, J., 1991a. Strain-rate and temperature dependence of the tensile flow stress of high-purity á-iron above 250 K (regime I) studied by means of stress-relaxation tests. Phys. Status Solidi (a) 124, 155–170.

Brunner, D., Diehl, J., 1991b. Temperature and strain-rate dependence of the tensile flow stress of high-purity α-iron below 250 K. I. Stress/temperature regime III. Phys. Status Solidi (a) 124, 455–464.

Brunner, D., Diehl, J., 1991c. Temperature and strain-rate dependence of the tensile flow stress of high-purity α-iron below 250 K II. Stress/temperature regime II and its transitions to regimes I and III. Phys. Status Solidi (a) 125, 203–216.

Buchheit, T., Battaile, C., Weinberger, C., Holm, E., 2011. Multi-scale modeling of low-temperature deformation in b.c.c. metals. JOM J. Miner. Metals Mater. Soc. 63, 33–36.

Caillard, D., 2010a. Kinetics of dislocations in pure Fe. Part I. In situ straining experiments at room temperature. Acta Mater. 58, 3493–3503.

Caillard, D., 2010b. Kinetics of dislocations in pure Fe. Part II. In situ straining experiments at low temperature. Acta Mater. 58, 3504–3515.

Chaussidon, J., Fivel, M., Rodney, D., 2006. The glide of screw dislocations in bcc Fe: Atomistic static and dynamic simulations. Acta Mater. 54, 3407–3416.

Chen, Z., 2013. Modelling the Plastic Deformation of Iron. KIT Scientific Publishing, Karlsruhe.

Chen, Z.M., Mrovec, M., Gumbsch, P., 2013. Atomistic aspects of ½ ⟨111⟩ screw dislocation behavior in α-iron and the derivation of microscopic yield criterion. Modell. Simul. Mater. Sci. Eng. 21, 055023.

Christian, J., 1983. Some surprising features of the plastic deformation of body-centered cubic metals and alloys. Metall. Mater. Trans. A 14, 1237–1256.

Dorn, J.E., Rajnak, S., 1964. Nucleation of kink pairs and the Peierls mechanism of plastic deformation. Trans. Metall. Soc. AIME 230, 1052–1064.

Duesbery, M.S., Vitek, V., 1998. Plastic anisotropy in b.c.c. transition metals. Acta Mater. 46, 1481–1492.

Gilbert, M.R., Queyreau, S., Marian, J., 2011. Stress and temperature dependence of screw dislocation mobility in α-Fe by molecular dynamics. Phys. Rev. B 84, 174103.

Gröger, R., Vitek, V., 2008. Multiscale modeling of plastic deformation of molybdenum and tungsten. III. Effects of temperature and plastic strain rate. Acta Mater. 56, 5426–5439.

Gröger, R., Bailey, A.G., Vitek, V., 2008a. Multiscale modeling of plastic deformation of molybdenum and tungsten: I. Atomistic studies of the core structure and glide of 1/2⟨111⟩ screw dislocations at 0 K. Acta Mater. 56, 5401–5411.

Gröger, R., Racherla, V., Bassani, J.L., Vitek, V., 2008b. Multiscale modeling of plastic deformation of molybdenum and tungsten: II. Yield criterion for single crystals based on atomistic studies of glide of screw dislocations. Acta Mater. 56, 5412–5425.

Irwin, G.J., Guiu, F., Pratt, P.L., 1974. The influence of orientation on slip and strain hardening of molybdenum single crystals. Phys. Status Solidi (a) 22, 685–698.

Johnson, R.A., Oh, D.J., 1989. Analytic embedded atom method model for bcc metals. J. Mater. Res. 4, 1195–1201.

Keh, A.S., 1965. Work hardening and deformation sub-structure in iron single crystals deformed in tension at 298°k. Philos. Mag. 12, 9–30.

Kocks, U.F., Argon, A.S., Ashby, M.F., 1975. Thermodynamics and Kinetics of Slip. Permagon Press, Progress in Materials Science.

Koester, A., Ma, A., Hartmaier, A., 2012. Atomistically informed crystal plasticity model for body-centered cubic iron. Acta Mater. 60, 3894–3901.

Li, D., Zbib, H., Sun, X., Khaleel, M., 2014. Predicting plastic flow and irradiation hardening of iron single crystal with mechanism-based continuum dislocation dynamics. Int. J. Plast. 52, 3–17.

Lim, H., Weinberger, C.R., Battaile, C.C., Buchheit, T.E., 2013. Application of generalized non-Schmid yield law to low-temperature plasticity in bcc transition metals. Modell. Simul. Mater. Sci. Eng. 21, 045015.

Marichal, C., Van Swygenhoven, H., Van Petegem, S., Borca, C., 2013. {110} slip with {112} slip traces in bcc Tungsten. Sci. Rep. 3.

Naamane, S., Monnet, G., Devincre, B., 2010. Low temperature deformation in iron studied with dislocation dynamics simulations. Int. J. Plast. 26, 84–92.

Narayanan, S., McDowell, D.L., Zhu, T., 2014. Crystal plasticity model for BCC iron atomistically informed by kinetics of correlated kinkpair nucleation on screw dislocation. J. Mech. Phys. Solids 65, 54–68.

Nawaz, M.H.A., Mordike, B.L., 1975. Slip geometry of tantalum and tantalum alloys. Phys. Status Solidi (a) 32, 449–458.

Patra, A., McDowell, D.L., 2012. Crystal plasticity-based constitutive modelling of irradiated bcc structures. Philos. Mag. 92, 861–887.

Qin, Q., Bassani, J.L., 1992a. Non-schmid yield behavior in single crystals. J. Mech. Phys. Solids 40, 813–833.

Qin, Q., Bassani, J.L., 1992b. Non-associated plastic flow in single crystals. J. Mech. Phys. Solids 40, 835–862.

Šesták, B., Zárubová, N., 1965. Asymmetry of slip in Fe-Si alloy single crystals. Phys. Status Solidi (b) 10, 239–250.

Spitzig, W., Keh, A., 1970a. Orientation and temperature dependence of slip in iron single crystals. Metall. Trans. 1, 2751–2757.

Spitzig, W., Keh, A., 1970b. Orientation dependence of the strain-rate sensitivity and thermally activated flow in iron single crystals. Acta Metall. 18, 1021–1033.

Spitzig, W., Keh, A., 1970c. The role of internal and effective stresses in the plastic flow of iron single crystals. Metall. Mater. Trans. B 1, 3325–3331.

Statham, C., Vesely, D., Christian, J., 1970. Slip in single crystals of niobium-molybdenum alloys deformed in compression. Acta Metall. 18, 1243–1252.

Stein, D., Low Jr., J., 1966. Effects of orientation and carbon on the mechanical properties of iron single crystals. Acta Metall. 14, 1183–1194.

Suzuki, T., Koizumi, H., Kirchner, H.O.K., 1995. Plastic flow stress of b.c.c. transition metals and the Peierls potential. Acta Metall. Mater. 43, 2177–2187.

Takeuchi, T., 1969. Orientation dependence of work-hardening in iron single crystals. Jpn. J. Appl. Phys. 8, 320–328.

Takeuchi, S., Furubayashi, E., Taoka, T., 1967. Orientation dependence of yield stress in 4.4% silicon iron single crystals. Acta Metall. 15, 1179–1191.

Van der Sluis, O., Schreurs, P.J.G., Brekelmans, W.A.M., Meijer, H.E.H., 2000. Overall behaviour of heterogeneous elastoviscoplastic materials: effect of microstructural modelling. Mech. Mater. 32, 449–462.

Vitek, V., 1992. Structure of dislocation cores in metallic materials and its impact on their plastic behaviour. Prog. Mater. Sci. 36, 1–27.

Vitek, V., 2004. Core structure of screw dislocations in body-centred cubic metals: relation to symmetry and interatomic bonding. Philos. Mag. 84, 415–428.

Vitek, V., Paidar, V., 2008. Chapter 87 Non-planar dislocation cores: a ubiquitous phenomenon affecting mechanical properties of crystalline materials. In: Hirth, J.P. (Ed.), Dislocations in Solids: A Tribute to F.R.N. Nabarro. Elsevier, pp. 439–514.

Vitek, V., Mrovec, M., Bassani, J.L., 2004a. Influence of non-glide stresses on plastic flow: from atomistic to continuum modeling. Mater. Sci. Eng., A 365, 31–37.

Vitek, V., Mrovec, M., Gröger, R., Bassani, J.L., Racherla, V., Yin, L., 2004b. Effects of non-glide stresses on the plastic flow of single and polycrystals of molybdenum. Mater. Sci. Eng., A 387–389, 138–142.

Weinberger, C.R., Battaile, C.C., Buchheit, T.E., Holm, E.A., 2012. Incorporating atomistic data of lattice friction into BCC crystal plasticity models. Int. J. Plast. 37, 16–30.

Yalcinkaya, T., Brekelmans, W.A.M., Geers, M.G.D., 2008. BCC single crystal plasticity modeling and its experimental identification. Modell. Simul. Mater. Sci. Eng. 16, 085007.

Zhu, T., Li, J., Yip, S., 2013. Atomistic reaction pathway sampling: the nudged elastic band method and nanomechanics applications. In: Horacio, D. (Ed.), Nano and Cell Mechanics: Fundamentals and Frontiers. Espinosa and Gang Bao, John Wiley & Sons, Chichester, UK, pp. 313–338.